Joint inversion of electromagnetic and acoustic data with edge-preserving regularization for breast imaging

Yingying Qin, Thomas Rodet, Dominique Lesselier, Marc Lambert

▶ **To cite this version:**

Yingying Qin, Thomas Rodet, Dominique Lesselier, Marc Lambert. Joint inversion of electromagnetic and acoustic data with edge-preserving regularization for breast imaging. IEEE Transactions on Computational Imaging, 2021, 7, pp.349-360. 10.1109/TCI.2021.3067158 . hal-02944427

HAL Id: hal-02944427

https://centralesupelec.hal.science/hal-02944427v1

Submitted on 7 Oct 2022

HAL is a multi-disciplinary open access archive for the deposit and dissemination of scientific research documents, whether they are published or not. The documents may come from teaching and research institutions in France or abroad, or from public or private research centers.

L'archive ouverte pluridisciplinaire **HAL**, est destinée au dépôt et à la diffusion de documents scientifiques de niveau recherche, publiés ou non, émanant des établissements d'enseignement et de recherche français ou étrangers, des laboratoires publics ou privés.

This is the author's version of an article that has been published in this journal. Changes were made to this version by the publisher prior to publication.
The final version of record is available at http://dx.doi.org/10.1109/TCI.2021.3067158

Joint inversion of electromagnetic and acoustic data with edge-preserving regularization for breast imaging

Yingying Qin, Thomas Rodet, Marc Lambert, and Dominique Lesselier *Senior Member IEEE*

***Abstract*—Joint inversion of microwave and ultrasonic data for breast imaging is investigated with deterministic edge-preserving regularization by introducing auxiliary variables indicating whether a pixel is on an edge or not. These edge markers are shared by dielectric and acoustic parameters and are the link to fusion between modalities. They can be jointly optimized from the last parameter profiles of microwave and ultrasonic cases and guide the next optimization as coefficients of the regularization term. Alternate minimization is used to update acoustic contrast, edge markers and dielectric contrast. Comprehensive numerical experiments are carried out on breast phantoms, a simple synthetic one and three extracted from a database. The results show, with comparisons to more classical approaches involving total variation or cross-gradient regularization developed in parallel, that the joint inversion algorithm can gain from the high resolution of ultrasonic imaging and the high contrast of microwave imaging. The quality of microwave imaging is enhanced in clear fashion and small tumors detected.**

***Index Terms*—breast imaging, microwave, ultrasound, data fusion, contrast source inversion, edge-preserving regularization**

I. Introduction

Breast cancer is common disease among females. X-ray mammography, as the standard for breast tumor detection, can provide high-resolution images. Yet, patients may suffer from ionizing radiation if too frequent examinations, and discomfort results from breast compression. Besides, the result is highly affected by breast density and exhibits low sensitivity.

Therefore, new imaging modalities with non-ionizing and low-cost features have been developed for breast tumor detection. Microwave imaging, due to the high contrast of the dielectric parameters between tumorous and normal tissues, has been investigated for breast imaging [1], [2]. However, images are of low resolution due to the long wavelength of the electromagnetic (EM) wave. In contrast, ultrasound (US) imaging, despite low contrast between different tissues, can provide high-resolution image and structure information [3], [4]. To take advantage of both modalities, inversion of electromagnetic and ultrasonic data in simultaneouly- or sequentially-combined fashion is expected to be fruitful.

Yet such a combination appears to still lack application in the field, beyond recent investigations, like [5] and references therein —possibly at prototype stage [6], with special embedding since within a closed metal chamber.

One way to exploit the pros of each modality is to extract structure information from high-resolution image. The authors have proposed such an approach in [7] based on the edge information. A reflectometric acoustic analysis is run to get the boundaries (possibly blurred) between zones in the breast. This information is employed to guide the smoothness constraint at each pixel: constraint will only be imposed on the pixels which are not on the edges pointed by the ultrasound image. Prior information based on regions is also investigated. After segmentation of high-resolution images, regions of different tissues can be obtained. Such information can give a better initial guess of the contrast at each pixel with parameters from literature and provide a finite element discretization for the reconstruction of dielectric parameters [5], [8].

Another way to combine multi-modalities is to invert the data simultaneously. To achieve joint inversion, physical relation between different parameters can be used and this leads to a unique retrieval of the underlying physical parameter. In [9], petrophysical relation is used for joint inversion of EM and seismic data. However, this option which relies on much *a priori* is not pursued further.

Structure similarity can be employed for joint inversion also. In [10], a Laplacian operator and two thresholds to measure the magnitude of the changes in parameters and minimize the difference of such parameters is investigated. In [11], [12], cross-gradient constraints as the outer product of the gradients of different parameters to force the parameters to change into the same direction are proposed. This method is widely used in geophysics [13]–[16]. In [17], Joint Total Variation for joint inversion by combining spatial gradients of both parameters as the weighting factor in the regularization term is considered. In [18], a Total-Variation-like regularization operator is to achieve joint inversion of EM and US data by changing the weight factor associated with the variation of the other modality. A review of joint inversion is found, e.g., in [17].

Considering that acoustic and dielectric parameters share discontinuities at the tissue boundaries and vary relatively smoothly within each tissue region, it is possible to constrain

Correspondance author: dominique.lesselier@l2s.centralesupelec.fr

Yingying Qin is with Université Paris-Saclay, ENS Paris-Saclay, CNRS, Systèmes et Applications des Technologies de l'Information et de l'Energie, 91190, Gif-sur-Yvette, France, and Université Paris-Saclay, CNRS, CentraleSupélec, Laboratoire des signaux et systèmes, 91190, Gif-sur-Yvette, France.

Thomas Rodet is with Université Paris-Saclay, ENS Paris-Saclay, CNRS, Systèmes et Applications des Technologies de l'Information et de l'Energie, 91190, Gif-sur-Yvette, France.

Marc Lambert is with Université Paris-Saclay, CentraleSupélec, CNRS, Laboratoire de Génie Electrique et Electronique de Paris, 91192, Gif-sur-Yvette, France.

Dominique Lesselier is with Université Paris-Saclay, CNRS, CentraleSupélec, Laboratoire des signaux et systèmes, 91190, Gif-sur-Yvette, France.

Copyright (c) 2021 IEEE. Personal use is permitted. For any other purposes, permission must be obtained from the IEEE by emailing pubs-permissions@ieee.org.

This is the author's version of an article that has been published in this journal. Changes were made to this version by the publisher prior to publication.
The final version of record is available at http://dx.doi.org/10.1109/TCI.2021.3067158

smoothness in the same region yet preserve edges at same location for parameters of two modalities to achieve joint inversion. Different functions [19]–[21] with edge-preserving property have been used in image reconstruction [22], [23], image restoration [24], image fusion [25] and many other tasks. In edge-preserving regularization [26], usually a nonquadratic function [27]–[29] is introduced to less severely penalize a large gradient to preserve edges. Duality between nonquadratic criterion and a half-quadratic (HQ) criterion with additional variables is observed, first with binary edge variables [30], [31], then generalized to continuous ones [32], [33].

With the augmented HQ criterion, the nonlinear optimization problem is transformed into a quadratic problem with respect to the original image and a nonquadratic but separable criterion for the edge variables. The problem is optimized by solving a sequence of sub-optimization problems to get the estimate of original image and edge map alternately [34]–[36]. With such a regularization, joint inversion can be achieved by introducing the common edge variables for both modalities and the sub-optimization problems are easy to solve.

In the present work, a new joint inversion algorithm of EM and US data is developed in a contrast source inversion (CSI) [37] framework with edge-preserving regularization. Hidden variables to indicate the parameter discontinuities in different directions are introduced, which connects inversions of US and EM data. Edge maps can be computed from the last parameter distribution and help the optimization at the next step. Alternate minimization is used to update acoustic contrast, edge maps and electromagnetic contrast.

In the numerical experiments, a pending breast —in contrast with the demanding compressed breast of X-ray mammography— immersed within an unbounded coupling medium is assumed. Several acoustic frequencies in the sub-MHz range (then associated to mm local wavelengths) provide a better estimation of edges, while a single electromagnetic frequency (1 GHz associated to cm local wavelengths) takes advantage of the high contrast while achieving enough penetration into the breast.

A 4-zone 2-D model of breast (skin, fatty, fibroglandular and tumor tissues) and four MRI-derived models from the UWCEM Breast Phantom Repository [38] are used to validate the algorithm, with application of a standard Method of Moments (Fast Fourier Transform being implemented in both forward and inverse problems to speed up the computations).

The contribution is organized as follows. In Section II the formulation of the forward problem is presented. In Section III, the joint inversion algorithm is detailed. In Section IV numerical experiments on breast phantoms are proposed. A brief conclusion follows in V.

II. Forward Problem

One considers a two-dimensional case. Time-harmonic waves are assumed with time dependence $\exp(-i\omega t)$ for both acoustic and electromagnetic cases. The modeled breast is located inside a domain of interest (DoI) $\mathcal{D}$. The known background medium is characterized by its complex relative permittivity ϵ_b, permeability μ_b, and wavenumber $k_b^{\text{em}} = \omega\sqrt{\epsilon_0\epsilon_b\mu_b}$ in electromagnetics, and its speed of sound c_b, attenuation α_b, and wavenumber $k_b^{\text{ac}} = \omega/c_b + i\alpha_b$ in acoustics. Permeability and density are taken constant within the DoI. The unknown parameters are complex relative permittivity $\epsilon_r(\mathbf{r}) = \epsilon_r'(\mathbf{r}) + i\epsilon_r''(\mathbf{r})$, sound speed $c(\mathbf{r})$ and attenuation $\alpha(\mathbf{r})$. For each imaging modality, N_i probes are evenly located at $\mathbf{r}_v'$, $v = 1, 2, \ldots, N_i$ on a circle $\mathcal{S}$, as shown in Figure 1. Each illuminates the DoI and scattered fields are collected by all.

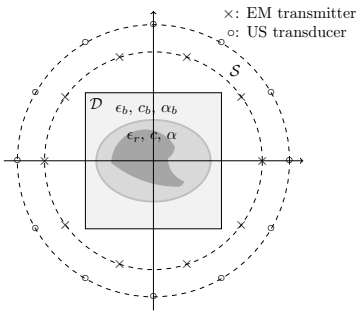

Fig. 1: Schematic diagram of configuration of two modalities working in a multistatic way

To solve the problem numerically, $\mathcal{D}$ is discretized into $M = X \times Y$ small cells centered at $\mathbf{r}_m$, $m = 1, 2, \ldots, M$. A pulse-basis point-matching method of moments (MoM) is employed. Every square cell is approximated by a small disk with same area and with equivalent radius R. Hereafter, $\overline{a}$ is used to denote a vector while $\overline{\overline{a}}$ a matrix. For the pth incidence, the fields inside $\mathcal{D}$ and on $\mathcal{S}$ can be described as

$$\overline{F}_p^t = \overline{F}_p^i + \overline{\overline{G}}_d \text{diag}(\overline{\chi})\overline{F}_p^t \tag{1}$$

$$\overline{F}_p^s = \overline{\overline{G}}_s \text{diag}(\overline{\chi})\overline{F}_p^t \tag{2}$$

where F is the pressure field P or the electric field E. Superscripts "i" and "t" denote incident and total field, i.e., the field inside $\mathcal{D}$ without and with breast, respectively. In this case, $\overline{F}_p^{i/t}$ is a $M \times 1$ vector with $\overline{F}_p^{i/t} = [F_p^{i/t}(\mathbf{r}_1), \ldots, F_p^{i/t}(\mathbf{r}_M)]^T$ where superscript "T" denotes transpose. $\overline{F}_p^s$ is a $N_i \times 1$ vector representing the scattered field collected by the receivers as $\overline{F}_p^s = [F_p^s(\mathbf{r}_1'), \ldots, F_p^s(\mathbf{r}_{N_i}')]^T$. Acoustic and electromagnetic contrasts read as

$$\chi^{\text{ac}}(\mathbf{r}) = \frac{(k^{\text{ac}}(\mathbf{r}))^2 - (k_b^{\text{ac}})^2}{(k_b^{\text{ac}})^2} \tag{3}$$

$$\chi^{\text{em}}(\mathbf{r}) = \frac{(k^{\text{em}}(\mathbf{r}))^2 - (k_b^{\text{em}})^2}{(k_b^{\text{em}})^2} \tag{4}$$

$M \times 1$ vector $\overline{\chi}$ is the discrete form of χ as $\overline{\chi} = [\chi(\mathbf{r}_1), \ldots, \chi(\mathbf{r}_M)]^T$.

$\overline{\overline{G}}_d$ is a $M \times M$ matrix with element

$$[\overline{\overline{G}}_d]_{m,m'} = \begin{cases} \dfrac{ik_b\pi R}{2} \mathrm{J}_1(k_b R)\, \mathrm{H}_0^{(1)}(k_b|\mathbf{r}_m - \mathbf{r}_{m'}|), m \neq m' \\ \dfrac{ik_b\pi R}{2} \mathrm{H}_1^{(1)}(k_b R) - 1, \text{otherwise} \end{cases} \tag{5}$$

where J_1 is the 1st-kind Bessel function, $\mathrm{H}_1^{(1)}$ the 1st-kind 1st-order Hankel function and $\mathrm{H}_0^{(1)}$ the 1st-kind 0th-order one.

Copyright (c) 2021 IEEE. Personal use is permitted. For any other purposes, permission must be obtained from the IEEE by emailing pubs-permissions@ieee.org.

This is the author's version of an article that has been published in this journal. Changes were made to this version by the publisher prior to publication.
The final version of record is available at http://dx.doi.org/10.1109/TCI.2021.3067158

The $N_i \times M$ matrix $\overline{\overline{G}}_s$ is

$$[\overline{\overline{G}}_s]_{v,m} = \frac{ik_b\pi R}{2} \mathrm{J}_1(k_b R)\, \mathrm{H}_0^{(1)}(k_b|\mathbf{r}'_v - \mathbf{r}'_m|) \tag{6}$$

Letting the contrast source be

$$J_p(\mathbf{r}) = \chi(\mathbf{r}) F_p^t(\mathbf{r}) \tag{7}$$

and multiplying by χ on both sides of previous equations, source-type equations in the discrete form follow as

$$\overline{J}_p = \mathrm{diag}(\overline{\chi})\overline{F}_p^i + \mathrm{diag}(\overline{\chi})\overline{\overline{G}}_d\overline{J}_p \tag{8}$$

$$\overline{F}_p^s = \overline{\overline{G}}_s\overline{J}_p \tag{9}$$

Based on those, a contrast source inversion (CSI) method can be developed and used in the proposed imaging procedure.

III. Inversion Algorithm

A. Deterministic edge-preserving regularization

Here, the edge-preserving regularization proposed in [26] is followed and only the main steps are shown (for further details and demonstrations, refer to the latter). Edge-preserving regularization enables to combine inversions of acoustic and electromagnetic data once assumed that discontinuities of corresponding properties occur at same locations. The regularization is imposed on the spatial gradients of the contrast. In this work, the first-order difference in horizontal, vertical and two diagonal directions are used and calculated as

$$[\overline{\overline{d}}_1]_{x,y} = \overline{\overline{\chi}}_{x,y} - \overline{\overline{\chi}}_{x,y+1} \tag{10}$$

$$[\overline{\overline{d}}_2]_{x,y} = \overline{\overline{\chi}}_{x,y} - \overline{\overline{\chi}}_{x+1,y} \tag{11}$$

$$[\overline{\overline{d}}_3]_{x,y} = (\overline{\overline{\chi}}_{x,y} - \overline{\overline{\chi}}_{x+1,y+1})/\sqrt{2} \tag{12}$$

$$[\overline{\overline{d}}_4]_{x,y} = (\overline{\overline{\chi}}_{x,y} - \overline{\overline{\chi}}_{x+1,y-1})/\sqrt{2} \tag{13}$$

with $[\overline{\overline{d}}_k]_{x,y}$, $k = 1, 2, 3, 4$, the spatial gradients for location (x, y). Here $X \times Y$ matrix $\overline{\overline{\chi}}$ is introduced and $\overline{\chi}$ is the vectorization of $\overline{\overline{\chi}}$ by column. For convenience, the above equations are written in matrix vector form as

$$\overline{\overline{D}}_k\overline{\chi} = \overline{d}_k \tag{14}$$

with $\overline{\overline{D}}_k$, $k = 1, 2, 3, 4$, the difference operators. Regularization is enforced separately on the real and imaginary parts of the spatial gradients at all pixels as

$$\begin{aligned} Q_{\mathrm{EP}}(\overline{\chi}) = \lambda_r \sum_k \sum_m^M \varphi\left(\frac{[\overline{\overline{D}}_k \Re\{\overline{\chi}\}]_m}{\delta_r}\right) \\ + \lambda_i \sum_k \sum_m \varphi\left(\frac{[\overline{\overline{D}}_k \Im\{\overline{\chi}\}]_m}{\delta_i}\right) \end{aligned} \tag{15}$$

Here, λ_r and λ_i are regularization parameters, and δ_r and δ_i are scaling parameters to determine the value of the discontinuity that can be detected. $\varphi(\cdot)$ is the potential function.

To simplify the minimization process, half-quadratic regularization [33] is carried out by introducing some auxiliary variables and the problem is transformed into $\mathrm{Min}_{\overline{\chi}} Q_{\mathrm{EP}}(\overline{\chi}) = \mathrm{Min}_{\overline{\chi},\overline{\overline{b}}} Q^*_{\mathrm{EP}}(\overline{\chi}, \overline{\overline{b}})$, with

$$\begin{aligned} Q^*_{\mathrm{EP}}(\overline{\chi}, \overline{\overline{b}}) = \lambda_r \sum_k \sum_m [\overline{b}_k]_m \left(\frac{[\overline{\overline{D}}_k \Re\{\overline{\chi}\}]_m}{\delta_r}\right)^2 + \psi\left([\overline{b}_k]_m\right) \\ + \lambda_i \sum_k \sum_m [\overline{b}_k]_m \left(\frac{[\overline{\overline{D}}_k \Im\{\overline{\chi}\}]_m}{\delta_i}\right)^2 + \psi\left([\overline{b}_k]_m\right) \end{aligned} \tag{16}$$

Additional variables $\overline{\overline{b}} = [\overline{b}_1, \overline{b}_2, \overline{b}_3, \overline{b}_4]$ indicate if the point is at an edge in detecting directions and their values are continuous in $[0, 1]$ with a small value for large gradients and vice versa. For the real and imaginary parts, they share the same edge markers. $\psi(\cdot)$ is a function determined by the potential function $\varphi(\cdot)$. When the contrast $\overline{\chi}$ is fixed, the value of $\overline{\overline{b}}$ can be calculated directly.

The potential function is chosen as $\varphi(t) = t^2/(1 + t^2)$ [29] and correspondingly $\psi(t) = t - 2\sqrt{t} + 1$. Even though the potential function is not convex, it can give a satisfactory imaging result in our experiment, also observed in [26].

B. Inversion of electromagnetic data with edge-preserving regularization

To better illustrate the joint algorithm, separate inversion with edge-preserving regularization is presented, taking the EM case as an example. For simplicity, the superscript "em" is omitted and $\overline{\overline{J}} = [\overline{J}_1, \ldots, \overline{J}_{N_i}]$ is used. Based on CSI, the cost function at the nth iteration is defined as

$$Q(\overline{\chi}, \overline{\overline{J}}, \overline{\overline{b}}) = Q_d(\overline{\overline{J}}) + Q_s(\overline{\overline{J}}, \overline{\chi}) + Q^*_{\mathrm{EP}}(\overline{\chi}, \overline{\overline{b}}) \tag{17}$$

with the normalized data equation and state equation errors being

$$Q_d = \frac{\sum_{p=1}^{N_i} \|\overline{E}_p^s - \overline{\overline{G}}_s\overline{J}_p\|^2}{\sum_{p=1}^{N_i} \|\overline{E}_p^s\|^2} \tag{18}$$

$$Q_s = \frac{\sum_{p=1}^{N_i} \|\mathrm{diag}(\overline{\chi})\overline{E}_p^i + \mathrm{diag}(\overline{\chi})\overline{\overline{G}}_d\overline{J}_p - \overline{J}_p\|^2}{\sum_{p=1}^{N_i} \|\mathrm{diag}(\overline{\chi}^{(n-1)})\overline{E}_p^i\|^2} \tag{19}$$

where $\overline{\chi}^{(n-1)}$ is the reconstruction result at the $(n-1)$th iteration.

To solve the above, the optimization procedures in [26] and [39] are followed and alternate minimization is run. The optimization procedure is summarized in Algorithm 1.

1) update $\overline{\overline{J}}$: At lth step, nth iteration, $\overline{\overline{J}}$ is updated by minimizing $Q = Q_d(\overline{\overline{J}}) + Q_s(\overline{\overline{J}}, \overline{\chi}^{(n-1)})$, which can be solved by gradient-based optimization methods. The partial gradient w.r.t. $\overline{J}_p$ is

$$\frac{\partial Q}{\partial \overline{J}_p} = -\frac{\overline{\overline{G}}_s^\dagger \overline{\rho}_p^{(n-1)}}{\sum_{p=1}^{N_i} \|\overline{E}_p^s\|^2} - \frac{\overline{o}_p^{(n-1)} - \overline{\overline{G}}_d^\dagger \mathrm{diag}(\overline{\chi}^{(n-1)})^\dagger \overline{o}_p^{(n-1)}}{\sum_{p=1}^{N_i} \|\mathrm{diag}(\overline{\chi}^{(n-1)})\overline{E}_p^i\|^2} \tag{20}$$

where superscript '†' denotes conjugate transpose. $\overline{o}_p^{(n-1)} = \mathrm{diag}(\overline{\chi}^{(n-1)})\overline{E}_p^i + \mathrm{diag}(\overline{\chi}^{(n-1)})\overline{\overline{G}}_d\overline{J}_p^{(n-1)} - \overline{J}_p^{(n-1)}$, and $\overline{\rho}_p^{(n-1)} = \overline{E}_p^s - \overline{\overline{G}}_s\overline{J}_p^{(n-1)}$.

Copyright (c) 2021 IEEE. Personal use is permitted. For any other purposes, permission must be obtained from the IEEE by emailing pubs-permissions@ieee.org.

This is the author's version of an article that has been published in this journal. Changes were made to this version by the publisher prior to publication.
The final version of record is available at http://dx.doi.org/10.1109/TCI.2021.3067158

Algorithm 1 Separate inversion with edge-preserving regularization

Input: $\overline{E}_p^s$, $\overline{E}_p^i$, $p = 1, \ldots, N_i$, $\overline{\overline{G}}_s$, $\overline{\overline{G}}_d$, regularization parameter λ_r, λ_i, δ_r, δ_i
Initialization: $\overline{\overline{J}}^{(0)}$, $\overline{\chi}^{(0)}$, step $l = 0$, iteration $n = 0$
repeat
  $l = l + 1$
  repeat
    $n = n + 1$
    With $\overline{\chi}^{(n-1)}$ and $\overline{\overline{b}}^{(l-1)}$, update $\overline{\overline{J}}$ by Equation (21)
    With $\overline{\overline{J}}^{(n)}$ and $\overline{\overline{b}}^{(l-1)}$, update $\overline{\chi}$ by Equation (22, 23)
  until a stopping criterion is satisfied
  With $\overline{\overline{J}}^{(n)}$ and $\overline{\chi}^{(n)}$, update $\overline{\overline{b}}$ by Equation (27)
until a stopping criterion is satisfied
Output: $\overline{\chi}$, $\overline{b}_1$, $\overline{b}_2$, $\overline{b}_3$, $\overline{b}_4$, $\overline{\overline{J}}$

With such a gradient, $\overline{J}_p$ is updated with the conjugate gradient method using the Polak-Ribière search direction as

$$\overline{J}_p^{(n)} = \overline{J}_p^{(n-1)} + \beta^{(n)} \overline{v}_p^{(n)} \tag{21}$$

where $\overline{v}_p^{(n)}$ is the search direction and $\beta^{(n)}$ the step size. More details are found in [39].

2) update $\overline{\chi}$: $\overline{\chi}$ is updated directly by minimizing $Q = Q_s(\overline{\overline{J}}^{(n)}, \overline{\chi}) + Q_{EP}^*(\overline{\chi}, \overline{\overline{b}}^{(l-1)})$. The solution can be obtained directly by letting $\partial Q / \partial \Re\{\overline{\chi}\} = 0$ and $\partial Q / \partial \Im\{\overline{\chi}\} = 0$, given as

$$\Re\{\overline{\chi}^{(n)}\} = (\overline{\overline{H}}^{(n)} + \lambda_r \overline{\overline{\Delta}}^{(l-1)} / \delta_r^2)^{-1} \Re\{\overline{z}^{(n)}\} \tag{22}$$

$$\Im\{\overline{\chi}^{(n)}\} = (\overline{\overline{H}}^{(n)} + \lambda_i \overline{\overline{\Delta}}^{(l-1)} / \delta_i^2)^{-1} \Im\{\overline{z}^{(n)}\} \tag{23}$$

where $\overline{\overline{H}}$ is a diagonal matrix with mth diagonal entry

$$\overline{\overline{H}}_m^{(n)} = \frac{\sum_p \|[\overline{E}_p^{t(n)}]_m\|^2}{\sum_p \|\mathrm{diag}(\overline{\chi}^{(n-1)}) \overline{E}_p^i\|^2} \tag{24}$$

with total field $\overline{E}_p^{t(n)} = \overline{E}_p^i + \overline{\overline{G}}_d \overline{J}_p^{(n)}$. $\overline{z}$ is a vector with mth entry

$$\overline{z}_m^{(n)} = \frac{\sum_p \mathrm{conj}([\overline{E}_p^{t(n)}]_m)[\overline{J}_p^{(n)}]_m}{\sum_p \|\mathrm{diag}(\overline{\chi}^{(n-1)}) \overline{E}_p^i\|^2} \tag{25}$$

and $\overline{\overline{\Delta}}$ is a matrix calculated by

$$\overline{\overline{\Delta}}^{(l-1)} = \sum_k (\overline{\overline{D}}_k)^T \mathrm{diag}(\overline{b}_k^{(l-1)}) \overline{\overline{D}}_k \tag{26}$$

3) update $\overline{\overline{b}}$: At the end of lth step, $\overline{\overline{b}}$ is updated by minimizing $Q = Q_{EP}^*(\overline{\chi}^{(n)}, \overline{\overline{b}})$. To remind, the potential function is $\varphi(t) = t^2/(1+t^2)$ and correspondingly $\psi(t) = t - 2\sqrt{t} + 1$. Letting $\partial Q / \partial \overline{b}_k = 0$, every element of $\overline{b}_k$ is obtained by

$$[\overline{b}_k^{(l)}]_m = \left(\frac{\lambda_r + \lambda_i}{\lambda_r + \lambda_i + (\overline{L}_k)_m} \right)^2 \tag{27}$$

where $\overline{L}_k$ is a vector with mth element

$$[\overline{L}_k]_m = \lambda_r \left(\frac{[\overline{\overline{D}}_k \Re\{\overline{\chi}^{(n)}\}]_m}{\delta_r} \right)^2 + \lambda_i \left(\frac{[\overline{\overline{D}}_k \Im\{\overline{\chi}^{(n)}\}]_m}{\delta_i} \right)^2 \tag{28}$$

In this work, initial guesses of $\overline{\overline{J}}$ and $\overline{\chi}$ are obtained by backpropagation [40]. The above algorithm can be employed also in the acoustic case, by changing electric field E and dielectric contrast $\overline{\chi}^{\mathrm{em}}$ to pressure field P and acoustic contrast $\overline{\chi}^{\mathrm{ac}}$ and changing regularization parameters $\lambda_{r/i}^{\mathrm{em}}$, $\delta_{r/i}^{\mathrm{em}}$ to $\lambda_{r/i}^{\mathrm{ac}}$ and $\delta_{r/i}^{\mathrm{ac}}$ accordingly.

C. Joint inversion of electromagnetic and acoustic data

Based on the assumption that dielectric and acoustic parameters share the same distribution of discontinuity, $\overline{\overline{b}}$ indicates edges for both parameters and is used to combine the modalities. The cost function for joint inversion is written as

$$\begin{aligned} Q = {} & Q_d(\overline{\overline{J}}^{\mathrm{em}}) + Q_s(\overline{\overline{J}}^{\mathrm{em}}, \overline{\chi}^{\mathrm{em}}) + Q_{\mathrm{EP}}^*(\overline{\chi}^{\mathrm{em}}, \overline{\overline{b}}) \\ & + \gamma \left(Q_d(\overline{\overline{J}}^{\mathrm{ac}}) + Q_s(\overline{\overline{J}}^{\mathrm{ac}}, \overline{\chi}^{\mathrm{ac}}) + Q_{\mathrm{EP}}^*(\overline{\chi}^{\mathrm{ac}}, \overline{\overline{b}}) \right) \end{aligned} \tag{29}$$

The regularization parameter γ is to balance the weight of acoustic and electromagnetic contrasts in calculating $\overline{\overline{b}}$.

Similar with separate inversion, alternate minimization is employed. In the optimization procedure, the cost function w.r.t. acoustic data is minimized first to obtain an initial estimate of $\overline{\overline{b}}$ to exhibit the discontinuities since acoustic imaging can indeed capture the fine structures. This value of $\overline{\overline{b}}$ is then used to obtain the electromagnetic image. Due to the large wavelength, the retrieval will be smoother, thus edges denoted by acoustic parameters caused by noise can be eliminated. The new $\overline{\overline{b}}$ is used in acoustic imaging again, and one works this way until convergence.

The joint inversion algorithm does not change the update of contrast current and contrast for both modalities compared with the separate inversion. Only the update of $\overline{\overline{b}}$ needs modification. At each step, $\overline{\overline{b}}$ is updated twice after the update of $\overline{\chi}^{\mathrm{ac}}$ and $\overline{\chi}^{\mathrm{em}}$, respectively. $\overline{\overline{b}}$ is updated by minimizing $Q = Q_{\mathrm{EP}}^*(\overline{\chi}^{\mathrm{ac}}, \overline{\overline{b}}) + \gamma Q_{\mathrm{EP}}^*(\overline{\chi}^{\mathrm{em}}, \overline{\overline{b}})$. The solution is

$$[\overline{b}_k]_m = \left(\frac{\gamma(\lambda_r^{\mathrm{em}} + \lambda_i^{\mathrm{em}}) + \lambda_r^{\mathrm{ac}} + \lambda_i^{\mathrm{ac}}}{\gamma \left(\lambda_r^{\mathrm{em}} + \lambda_i^{\mathrm{em}} + [\overline{L}_k^{\mathrm{em}}]_m \right) + \lambda_r^{\mathrm{ac}} + \lambda_i^{\mathrm{ac}} + [\overline{L}_k^{\mathrm{ac}}]_m} \right)^2 \tag{30}$$

where $\overline{L}_k^{\mathrm{em/ac}}$ is given in Equation (28) with corresponding regularization parameters and contrast.

Notice that $\gamma = 0$ for the first update of $\overline{\overline{b}}$, which means that only acoustic parameters are used at the start.

The whole optimization procedure is sketched in Algorithm 2. One stops the update of contrast when the relative difference in contrast is less than some threshold θ and one stops the whole optimization when the change of electromagnetic contrast in two successive steps is less than θ, or when the maximum iteration number is reached.

Copyright (c) 2021 IEEE. Personal use is permitted. For any other purposes, permission must be obtained from the IEEE by emailing pubs-permissions@ieee.org.

This is the author's version of an article that has been published in this journal. Changes were made to this version by the publisher prior to publication.
The final version of record is available at http://dx.doi.org/10.1109/TCI.2021.3067158

Algorithm 2 Joint inversion with edge-preserving regularization

Input: $\overline{E}_p^s$, $\overline{E}_p^i$, $\overline{P}_p^s$, $\overline{P}_p^i$, $p = 1, \ldots, N_i$, $\overline{\overline{G}}_s^{\text{em}}$, $\overline{\overline{G}}_d^{\text{em}}$, $\overline{\overline{G}}_s^{\text{ac}}$, $\overline{\overline{G}}_d^{\text{ac}}$, regularization parameters γ, λ_r^{ac}, λ_i^{ac}, λ_r^{em}, λ_i^{em}, δ_r^{ac}, δ_i^{ac}, δ_r^{em}, δ_i^{em}

Initialization: $\overline{\chi}^{\text{ac}(0)}$, $\overline{\chi}^{\text{em}(0)}$, $\overline{\overline{J}}^{\text{ac}(0)}$, $\overline{\overline{J}}^{\text{em}(0)}$

repeat
  repeat
    Update $\overline{\overline{J}}^{\text{ac}}$ with Equation (21)
    Update $\overline{\chi}^{\text{ac}}$ with Equations (22) and (23)
  until a stopping criterion is satisfied
  Update $\overline{b}_1$, $\overline{b}_2$, $\overline{b}_3$, $\overline{b}_4$, with Equation (30)
  repeat
    Update $\overline{\overline{J}}^{\text{em}}$ with Equation (21)
    Update $\overline{\chi}^{\text{em}}$ with Equations (22) and (23)
  until a stopping criterion is satisfied
  Update $\overline{b}_1$, $\overline{b}_2$, $\overline{b}_3$, $\overline{b}_4$, with Equation (30)
until a stopping criterion is satisfied
Output $\overline{\chi}^{\text{ac}}$, $\overline{\chi}^{\text{em}}$, $\overline{b}_1$, $\overline{b}_2$, $\overline{b}_3$, $\overline{b}_4$, $\overline{\overline{J}}^{\text{ac}}$, $\overline{\overline{J}}^{\text{em}}$

IV. Numerical experiments

In this section, numerical experiments are conducted on several breast models. First the algorithm is validated on a synthetic model with regular tissue shapes, then is investigated on three realistic breast models which have more complicated inner structures. All simulations are run on Matlab R2018b.

In the simulation, for the electromagnetic case, 40 antennas are evenly set on a circle, working as sources and receivers simultaneously at a single 1 GHz operation frequency.

For the acoustic case, 64 transducers operate at three frequencies, namely 100, 150 and 200 kHz, to get a better estimate of the structure in the first step. Considering the acoustic wavenumber $k^{\text{ac}} = \omega/c + i\alpha$ wherein attenuation $\alpha = \alpha_0 f$, α_0 the attenuation at frequency f =1 MHz (here a linear dependence is assumed [41]), the approximation can be made that the acoustic contrast does not change with frequency.

The DoI is discretized by MoM into a grid which is at least twice finer than the one used in inversion. The synthetic data are obtained by solving the forward problem with two steps: first, the contrast current is calculated by solving Equation 8 with a conjugate-gradient fast Fourier transform (CG-FFT) algorithm, then, the scattered field is obtained directly based on Equation 9. Additive Gaussian noise is added to the data.

For the inversion, the breast is assumed known to be in a given disk. The reconstruction is confined within this region and pixels outside it are restricted to have the same dielectric and acoustic properties as those of the coupling medium. Besides, the dielectric and acoustic parameters are bounded as $1 \leqslant \epsilon_r' \leqslant 70$, $0 \leqslant \epsilon_r'' \leqslant 40$, $1200 \leqslant c \leqslant 1800$, and $0 \leqslant \alpha \leqslant 5$ at each iteration by a projection method.

Two separate inversion and one joint inversion algorithms are run for comparison: CSI with deterministic edge-preserving regularization (CSI-EP) described in Section III-B, CSI with multiplicative weighted L^2-norm total variation (MR-CSI) [42], [43] and cross-gradient function [16] as a joint inversion method incorporated in CSI (JCSI-CG).

TABLE I: Acoustic sound speed in m/s and attenuation in dB/MHz/cm, and relative dielectric permittivity ϵ_r at 1 GHz, for different tissues and background.

Tissue/Media	sound speed c	attenuation α_0	permittivity ϵ_r
skin	1615	0.35	$39.8816 + 15.6363i$
fatty	1478	0.48	$4.7950 + 0.8185i$
glandular	1510	0.75	$48.8218 + 15.8941i$
tumor	1548	1.45	$56.2672 + 17.9652i$
background	1568	0.056	$10 + 4i$

Imaging quality is evaluated in quantitative fashion via the relative error between reconstructed parameters $\overline{\zeta}$ and ground truth $\overline{\xi}$ calculated as

$$\text{Err} = \frac{\|\overline{\zeta} - \overline{\xi}\|_2}{\|\overline{\xi}\|_2} \tag{31}$$

and via the Structural Similarity (SSIM) Index [44]

$$\text{SSIM} = \frac{(2\mu_\zeta\mu_\xi + C_1)(2\sigma_{\zeta\xi} + C_2)}{(\mu_\zeta^2 + \mu_\xi^2 + C_1)(\sigma_\zeta^2 + \sigma_\xi^2 + C_2)} \tag{32}$$

where μ_ζ and σ_ζ are the mean and standard deviation of $\overline{\zeta}$, respectively. $\sigma_{\zeta\xi}$ is the covariance between $\overline{\zeta}$ and $\overline{\xi}$. $C_1 = (K_1 L)^2$ and $C_2 = (K_2 L)^2$ are used to avoid instability. In our calculation, $K_1 = 0.01$, $K_2 = 0.03$, $L = 70$, 40, 600 and 5 are set for ϵ_r', ϵ_r'', c and α respectively.

A. Reconstruction of synthetic breast model

Model 1 is a simple synthetic breast model which consists of skin, fatty, fibroconnective/glandular and tumorous tissues. Each tissue type has regular shape and uniform dielectric property. The skin thickness is 2 mm and the tumor is of 6 mm-diameter. In this model, the DoI is $0.1\,\text{m} \times 0.1\,\text{m}$-sized.

Acoustic and dielectric parameters of tissue types [2], [41], [45] and coupling medium are in Table I. Figure 2 (1st column) shows the distribution of sound speed, attenuation, real and imaginary parts of the relative permittivity of this model.

The EM antennas are set on a circle of $0.057\,\text{m}$ radius, the US transducers on one of $0.08\,\text{m}$ radius. The DoI is discretized into 200×200 pixels for the electromagnetic case and 350×350 pixels for the acoustic one. Gaussian noise with SNR = 30 dB is added to the synthetic data.

For the inversion, the domain is discretized into 80×80 pixels. The breast is assumed within a disk of $0.045\,\text{m}$ radius (the radius of the outer boundary of the model is $0.042\,\text{m}$).

The hyperparameter δ controls the discontinuity that can be detected, λ is to balance the trade-off between data and regularization terms, and γ to control the weight of acoustic and electromagnetic data when updating edge maps. Numerical experimentation provides their values as follows.

δ is chosen as $\delta_r^{\text{ac}} = \delta_i^{\text{ac}} = 5 \times 10^{-3}$, $\delta_r^{\text{em}} = 10^{-1}$ and $\delta_i^{\text{em}} = 10^{-2}$. $\delta_i^{\text{ac}} = \delta_r^{\text{ac}}$ is as such since the reconstruction of attenuation is usually not satisfactory and one attempts to

Copyright (c) 2021 IEEE. Personal use is permitted. For any other purposes, permission must be obtained from the IEEE by emailing pubs-permissions@ieee.org.

This is the author's version of an article that has been published in this journal. Changes were made to this version by the publisher prior to publication.
The final version of record is available at http://dx.doi.org/10.1109/TCI.2021.3067158

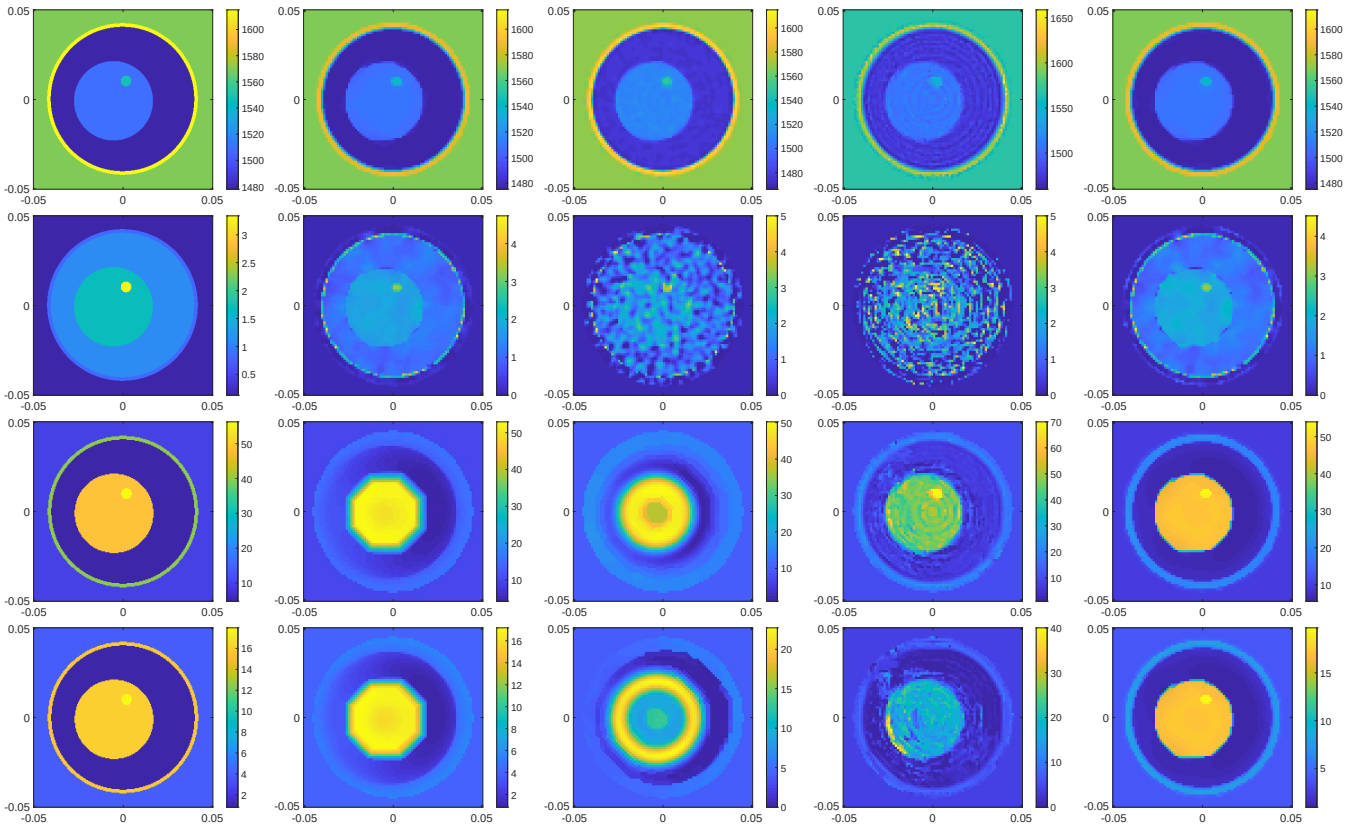

Fig. 2: Model 1 – Ground truth (1st column), separate reconstruction results of CSI-EP (2nd), MR-CSI (3rd) and joint inversion results of JCSI-CG (4th) and JCSI-EP (5th) with speed of sound c (1st row), attenuation α (2nd), real part ϵ_r' (3rd) and imaginary part ϵ_r'' (4th) of relative permittivity.

decrease the effect of attenuation on calculating $\overline{\overline{b}}$. $\lambda_r = \lambda_i$ is simply set for both acoustic and electromagnetic cases with $\lambda^{\text{ac}} = 5 \times 10^{-7}$ and $\lambda^{\text{em}} = 5 \times 10^{-7}$. $\gamma = 0.5$ is set to give comparable weights to electromagnetic and acoustic contrasts. As for the threshold θ in the stopping criterion, it must be small enough to maintain accuracy, yet not too small to avoid lengthy computations, and it is taken as 10^{-3}.

Figure 2 (2nd and 3rd columns) shows the separate inversion results of two modalities by CSI-EP with the same regularization parameter values and MR-CSI. The speed of sound can be well retrieved by both algorithms, yet the dielectric parameters are more difficult to estimate while the tumor cannot be seen for either one.

Results of JCSI-CG and proposed JCSI-EP are shown in the 4th and 5th columns. Compared with separate inversion, the tumor can be clearly seen in the real part of dielectric parameter profiles in both joint inversion algorithms and the quality of EM reconstruction is enhanced. Our algorithm also has a better reconstruction result of the imaginary part than JCSI-CG on this model. Besides, the noise is well smoothed.

Figure 3 displays the edge variables at different steps of JCSI-EP algorithm. The edges are well retrieved. After the first update, the edge map is not accurate but as the optimization proceeds, the edges becomes sharper and the noise is smoothed.

The assessment results associated with the algorithms above are shown in Table II. Though acoustic imaging benefits little from joint inversion, it appears that the quality of microwave imaging can be greatly improved. In particular, the proposed algorithm yields a smaller relative error and a higher SSIM value compared with cross-gradient method.

TABLE II: Model 1 – Imaging quality assessment in the reconstruction of acoustic and dielectric parameters

Index	Methods	acoustic parameter		dielectric parameter	
		c	α	ϵ_r'	ϵ_r''
Err	CSI-EP	0.0077	**0.3370**	0.3619	0.4004
	MR-CSI	**0.0061**	0.5653	0.3808	0.7233
	JCSI-CG	0.0080	0.8900	0.2971	0.4596
	JCSI-EP	0.0078	0.3406	**0.2664**	**0.3002**
SSIM	CSI-EP	0.9667	**0.8834**	0.8498	0.8163
	MR-CSI	**0.9794**	0.7237	0.8166	0.5097
	JCSI-CG	0.9649	0.5148	0.9001	0.8077
	JCSI-EP	0.9655	0.8798	**0.9198**	**0.9088**

B. Reconstruction of realistic breast phantoms

To better validate the proposed approach, experiments are conducted on several more realistic breast models, which are slices extracted from breast phantoms in the UWCEM repository [38] and are categorized in different classes according to radiographic density. The grid size is $0.5\,\text{mm}$ and it is used in simulations for generation of synthetic data in both acoustic and electromagnetic cases. The thickness of skin is changed

Copyright (c) 2021 IEEE. Personal use is permitted. For any other purposes, permission must be obtained from the IEEE by emailing pubs-permissions@ieee.org.

This is the author's version of an article that has been published in this journal. Changes were made to this version by the publisher prior to publication.
The final version of record is available at http://dx.doi.org/10.1109/TCI.2021.3067158

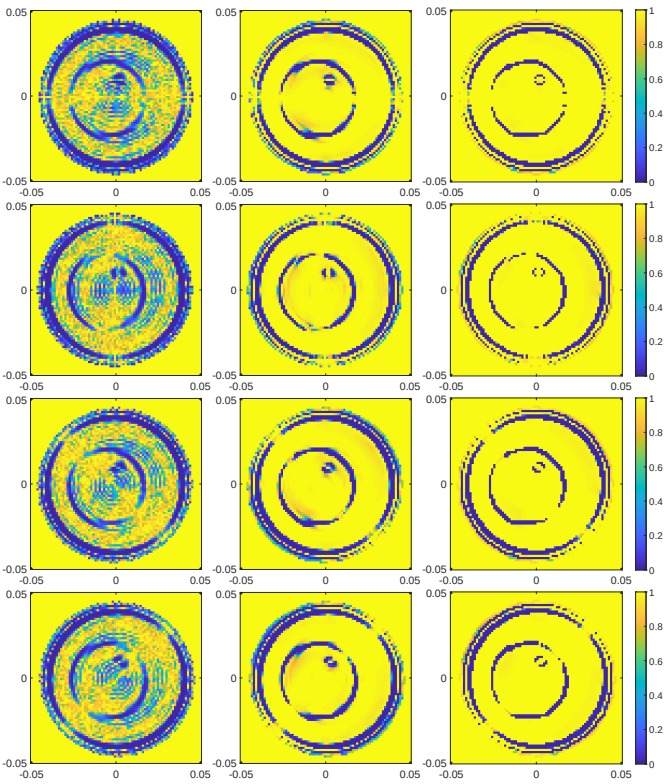

Fig. 3: Model 1 - Joint reconstruction of edge variables b_x, b_y, d_{d1} and b_{d2} (from top to bottom) after 1st, 5th and 40th update (from left to right).

TABLE III: Model 2 – Imaging quality assessment in the reconstruction of acoustic and dielectric parameters

Index	Methods	acoustic parameter c	acoustic parameter α	dielectric parameter ϵ_r'	dielectric parameter ϵ_r''
Err	CSI-EP	**0.0097**	0.3915	0.4808	0.5901
	MR-CSI	0.0098	0.6413	0.4715	0.5750
	JCSI-CG	0.0100	0.9070	0.4473	0.5619
	JCSI-EP ($\gamma = 0$)	0.0097	0.3915	**0.4406**	**0.4640**
	JCSI-EP ($\gamma = 0.5$)	0.0097	0.3977	0.4411	0.4771
	JCSI-EP ($\gamma = 5$)	0.0099	**0.3763**	0.4486	0.4856
SSIM	CSI-EP	0.9424	0.8718	0.6446	0.5323
	MR-CSI	**0.9426**	0.7113	0.6768	0.5414
	JCSI-CG	0.9404	0.5558	0.7164	0.6107
	JCSI-EP($\gamma = 0$)	0.9424	0.8718	0.7129	**0.7019**
	JCSI-EP($\gamma = 0.5$)	0.9420	0.8678	**0.7221**	0.6946
	JCSI-EP($\gamma = 5$)	0.9420	**0.8796**	0.7143	0.6777

TABLE IV: Model 2 – Imaging quality assessment in acoustic and dielectric parameters with different SNR

Index	SNR (dB) AC	SNR (dB) EM	acoustic parameter c	acoustic parameter α	dielectric parameter ϵ_r'	dielectric parameter ϵ_r''
Err	10	10	0.0131	1.0786	0.4770	0.5226
	10	30	0.0130	1.0697	0.4719	0.5157
	30	10	0.0098	**0.3934**	0.4436	0.4828
	30	30	**0.0097**	0.3977	**0.4411**	**0.4771**
SSIM	10	10	0.9002	0.0183	0.6844	0.6347
	10	30	0.9010	0.0212	0.6831	0.6380
	30	10	0.9410	**0.8707**	0.7218	0.6932
	30	30	**0.9420**	0.8678	**0.7221**	**0.6946**

from $1.5\,\mathrm{mm}$ to $2\,\mathrm{mm}$. The acoustic parameters are the same as with Model 1 and assigned according to the tissue type of each pixel and the type "transitional" is given the average value of fatty and glandular tissues. The Debye parameters of dielectric properties for normal tissues are from [2]. As for the hypothesized antennas, they are set on a circle of $0.08\,\mathrm{m}$ radius and the transducers on one of $0.1\,\mathrm{m}$ radius.

To test resolution of the separate and joint procedures, a synthetic tumor is added into each model and the relative permittivity is chosen as the 75th percentile curve in [46].

For inversion, a cell size of $2\,\mathrm{mm}$ is adopted. Notice that some columns or rows of pixels are added as background in the initial breast phantoms to make the numbers of columns and rows multiples of 4. The region of the breast is also assumed known with a three-pixel margin left.

In this section, δ is kept unchanged as $\delta_r^{\mathrm{ac}} = \delta_i^{\mathrm{ac}} = 5\times10^{-3}$, $\delta_r^{\mathrm{em}} = 10^{-1}$ and $\delta_i^{\mathrm{em}} = 10^{-2}$. The regularization parameters are chosen as $\lambda^{\mathrm{em}} = 2 \times 10^{-6}$ and $\lambda^{\mathrm{ac}} = 2 \times 10^{-6}$ for all breast phantoms. The threshold in the stopping criterion is $\theta = 5 \times 10^{-4}$. Two levels of SNR are considered: $30\,\mathrm{dB}$ and $10\,\mathrm{dB}$. The effect of γ is studied for different phantoms. Three values of γ are set as $\gamma = 0$, 0.5 and 5.

1) Class 3 model: The first phantom (ID 080304, slice s_1=150) is heterogeneously dense. Two models are developed from this phantom. The slice contains 332×204 pixels for simulation and 83×51 pixels for inversion. In Model 2, a synthetic 1 cm-diameter tumor at position $(1.2\,\mathrm{cm}, -0.5\,\mathrm{cm})$ is inserted while in Model 3, a tumor with an irregular shape is considered at same location.

Figures 4 and 5 (1st column) show the distributions of acoustic and electromagnetic parameters of these two models. With noise of $30\,\mathrm{dB}$, separate reconstruction results of CSI-EP, MR-CSI and joint inversion results of JCSI-CG and JCSI-EP with $\gamma = 0.5$ for these two models are also shown. Similarly, in separate imaging, the speed of sound can be retrieved well, while the results of dielectric parameters are unsatisfactory. The tumor cannot be identified and the results of these two models are quite similar.

JCSI-CG can image the tumor with a slight distortion in the real part of relative permittivity of Model 2, but in Model 3, the imaging result gets worse and the tumor is almost indistinguishable. Still, the imaginary parts are unsatisfactory and cannot estimate the tissue structures well. In contrast, the tumor can be well identified in all parameters with JCSI-EP for both models. The skin is difficult to image since only one-pixel wide. The difference in the shape of tumor can also be seen when comparing the results of these two models, and the shapes fit the ground truth.

The effect of regularization parameter γ is also investigated. These two models have quite similar results and Figure 6 shows the results of Model 3 by JCSI-EP with $\gamma = 0$, 0.5 and 5. As γ increases, the contrast between the tumor and the background becomes lower. The tumor can still be seen in all cases and overall the results are satisfactory.

Table III and V show the quantitative assessment of the imaging quality. Joint inversion algorithms have a better reconstruction than separate ones in dielectric parameters.

Copyright (c) 2021 IEEE. Personal use is permitted. For any other purposes, permission must be obtained from the IEEE by emailing pubs-permissions@ieee.org.

This is the author's version of an article that has been published in this journal. Changes were made to this version by the publisher prior to publication.
The final version of record is available at http://dx.doi.org/10.1109/TCI.2021.3067158

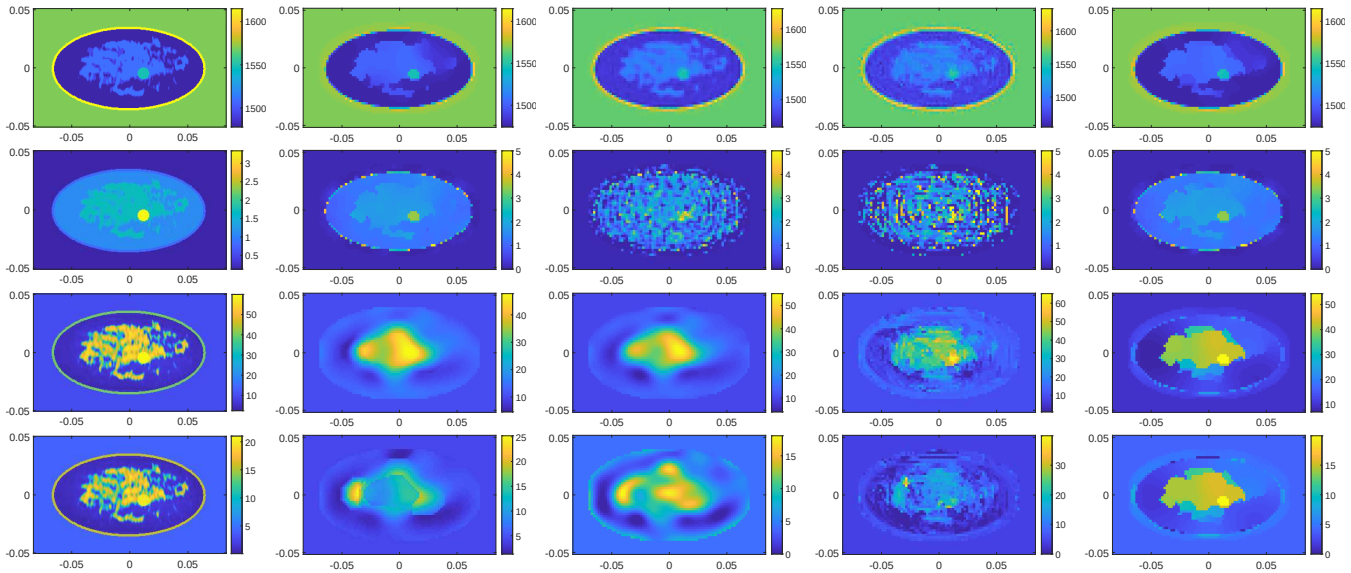

Fig. 4: Model 2 – Ground truth (1st column), separate reconstruction results of CSI-EP (2nd), MR-CSI (3rd) and joint inversion results of JCSI-CG, JCSI-EP (5th) with speed of sound c (1st row), attenuation α (2nd), real part ϵ_r' (3rd) and imaginary part ϵ_r'' (4th) of relative permittivity.

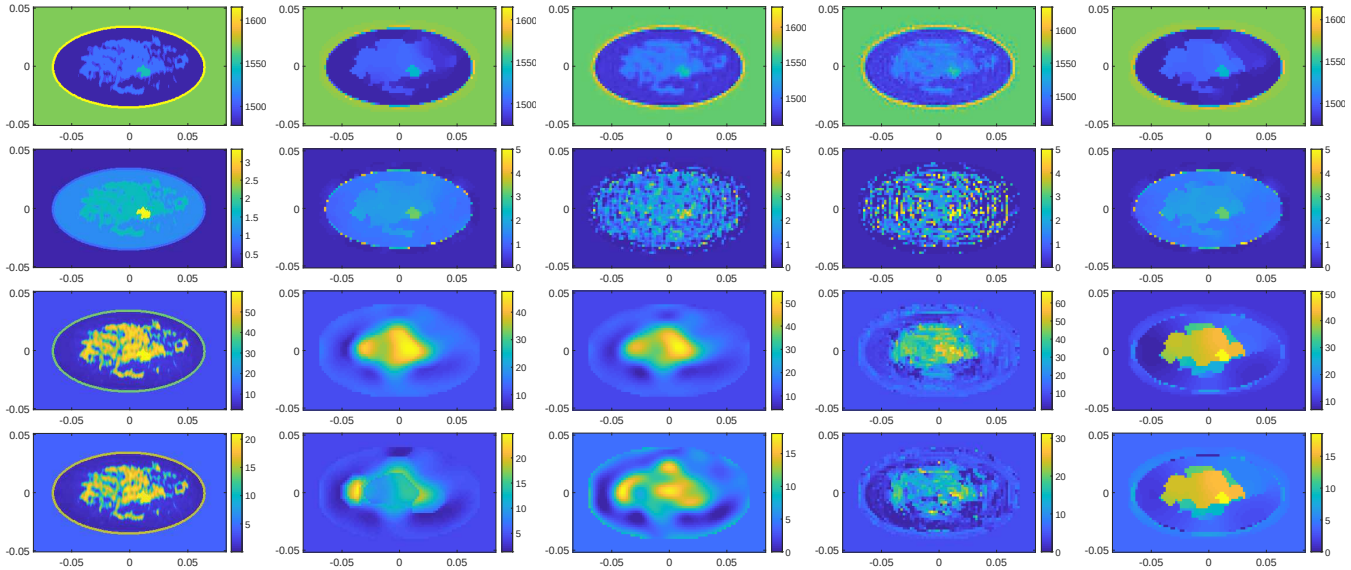

Fig. 5: Model 3 – Ground truth (1st column), separate reconstruction results of CSI-EP (2nd), MR-CSI (3rd) and joint inversion results of JCSI-CG (4th) and JCSI-EP (5th) with speed of sound c (1st row), attenuation α (2nd), real part ϵ_r' (3rd) and imaginary part ϵ_r'' (4th) of relative permittivity.

JCSI-CG has a higher SSIM value in the real part of the dielectric parameter but the smallest value in the imaginary part among all the joint inversion results. JCSI-EP with $\gamma = 0$ has the smallest relative error in dielectric parameters for both models which may be because the dielectric parameters are not uniform in each region and combining EM data may oversmooth the reconstruction result.

With $\gamma = 0.5$, the imaging quality with different levels of noise are given in Tables IV and VI. As can be seen from the tables, a decrease in SNR of acoustic data can result in a more severe degradation in imaging quality than with electromagnetic data. Thus, a high quality of acoustic data is needed for a satisfactory result. Since the hyperparameters are fixed for all breast phantoms, this choice may be not optimal for every one. Therefore, as shown in Table VI, a lower SNR of electromagnetic data may lead to a better result than the one obtained with a higher SNR.

2) Class 4 model: The phantom (ID 012304, slice s_1=100) is very dense. The slice contains 328×212 pixels for the forward problem, 82×53 pixels for inversion. In Model 4, a synthetic tumor of irregular shape is added at $(1.8\,\mathrm{cm}, 1.2\,\mathrm{cm})$.

Figure 7 shows the distributions of acoustic and electromagnetic parameters and the reconstruction results of different algorithms and Figure 8 compares the results with different

Copyright (c) 2021 IEEE. Personal use is permitted. For any other purposes, permission must be obtained from the IEEE by emailing pubs-permissions@ieee.org.

This is the author's version of an article that has been published in this journal. Changes were made to this version by the publisher prior to publication.
The final version of record is available at http://dx.doi.org/10.1109/TCI.2021.3067158

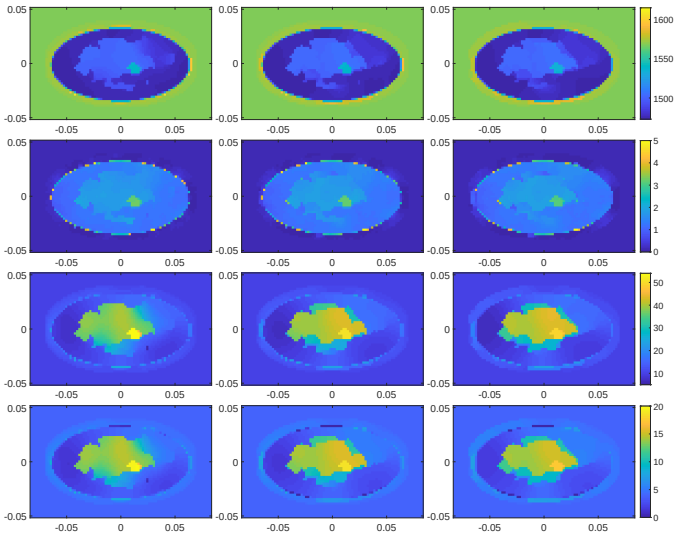

Fig. 6: Model 3 – Joint reconstruction results of speed of sound c (1st row), attenuation α (2nd), real part ϵ_r' (3rd) and imaginary part ϵ_r'' (4th) of relative permittivity by JCSI-EP with $\gamma = 0$ (left), $\gamma = 0.5$ (middle) and $\gamma = 5$ (right).

TABLE V: Model 3 – Imaging quality assessment in the reconstruction of acoustic and dielectric parameters

Index	Methods	acoustic parameter c	acoustic parameter α	dielectric parameter ϵ_r'	dielectric parameter ϵ_r''
Err	CSI-EP	**0.0097**	0.3927	0.4805	0.5890
	MR-CSI	0.0098	0.6377	0.4712	0.5741
	JCSI-CG	0.0101	0.9620	0.4445	0.5822
	JCSI-EP ($\gamma = 0$)	0.0097	0.3927	**0.4421**	**0.4658**
	JCSI-EP ($\gamma = 0.5$)	0.0098	0.3983	0.4430	0.4811
	JCSI-EP ($\gamma = 5$)	0.0099	**0.3807**	0.4498	0.4894
SSIM	CSI-EP	0.9419	0.8708	0.6443	0.5325
	MR-CSI	**0.9425**	0.7141	0.6768	0.5415
	JCSI-CG	0.9394	0.5289	**0.7260**	0.5946
	JCSI-EP($\gamma = 0$)	0.9419	0.8708	0.7088	**0.6977**
	JCSI-EP($\gamma = 0.5$)	0.9411	0.8672	0.7172	0.6862
	JCSI-EP($\gamma = 5$)	0.9400	**0.8765**	0.7091	0.6685

TABLE VI: Model 3 – Imaging quality assessment in acoustic and dielectric parameters with different SNR

Index	SNR (dB) AC	SNR (dB) EM	acoustic parameter c	acoustic parameter α	dielectric parameter ϵ_r'	dielectric parameter ϵ_r''
Err	10	10	0.0126	1.0036	0.4689	0.5100
	10	30	0.0125	0.9991	0.4692	0.5145
	30	10	**0.0098**	**0.3962**	0.4432	**0.4767**
	30	30	0.0098	0.3983	**0.4430**	0.4811
SSIM	10	10	0.9081	0.0293	0.6868	0.6452
	10	30	0.9083	0.0294	0.6811	0.6384
	30	10	0.9408	**0.8685**	**0.7225**	**0.6944**
	30	30	**0.9411**	0.8672	0.7172	0.6862

TABLE VII: Model 4 – Imaging quality assessment in the reconstruction of acoustic and dielectric parameters

Index	Methods	acoustic parameter c	acoustic parameter α	dielectric parameter ϵ_r'	dielectric parameter ϵ_r''
Err	CSI-EP	**0.0089**	0.3521	0.4505	0.5861
	MR-CSI	0.0090	0.5817	0.4391	0.5576
	JCSI-CG	0.0093	0.8499	0.4285	0.6591
	JCSI-EP ($\gamma = 0$)	0.0089	0.3523	0.4160	**0.4415**
	JCSI-EP ($\gamma = 0.5$)	0.0089	0.3513	**0.4157**	0.4523
	JCSI-EP ($\gamma = 5$)	0.0089	**0.3258**	0.4158	0.4544
SSIM	CSI-EP	0.9429	0.9056	0.6872	0.5449
	MR-CSI	**0.9433**	0.7739	0.7206	0.5813
	JCSI-CG	0.9398	0.6215	0.7423	0.5020
	JCSI-EP($\gamma = 0$)	0.9429	0.9056	0.7473	**0.7265**
	JCSI-EP($\gamma = 0.5$)	0.9432	0.9056	**0.7495**	0.7246
	JCSI-EP($\gamma = 5$)	0.9428	**0.9173**	0.7492	0.7192

TABLE VIII: Model 4 – Imaging quality assessment in the reconstruction of acoustic and dielectric parameters with different SNR

Index	SNR (dB) AC	SNR (dB) EM	acoustic parameter c	acoustic parameter α	dielectric parameter ϵ_r'	dielectric parameter ϵ_r''
Err	10	10	0.0108	1.0097	0.4427	0.4764
	10	30	0.0108	1.0262	0.4429	0.4817
	30	10	**0.0089**	**0.3502**	**0.4134**	**0.4473**
	30	30	0.0089	0.3513	0.4157	0.4523
SSIM	10	10	0.9189	0.1374	0.7356	0.6982
	10	30	0.9189	0.1335	0.7159	0.6813
	30	10	0.9412	0.8685	**0.7523**	**0.7361**
	30	30	**0.9432**	**0.9056**	0.7495	0.7246

values of γ. The quality assessment is given in Table VII.

As before, in separate inversion, the speed of sound can be reconstructed well and fine structures can be identified in the acoustic case, but the reconstructions of dielectric parameters are not satisfactory and the tumor cannot be seen.

Joint inversion algorithms have improved the reconstruction of dielectric parameters. In detail, JCSI-CG can show the structure of glandular part but the tumor is not obvious in dielectric parameters, while JCSI-EP can give a better estimate of the location and shape of the tumor. According to the quantitative assessment, JCSI-EP performs best in the reconstruction of real part of relative permittivity when $\gamma = 0.5$, while for the imaginary part, $\gamma = 0$ gives the best result. When $\gamma = 5$, the images of JCSI-EP are oversmoothed and the tumor cannot emerge well from the dielectric parameters while in the other cases the tumor can be identified clearly and the overall results are satisfactory.

Table VIII provides the quality assessment with different levels of noise with $\gamma = 0.5$. As with the results above, the noise level of acoustic data has a higher influence on the final result. A relative low level of noise is needed for successful tumor detection.

V. Conclusion

In the present work, a joint inversion algorithm of electromagnetic and acoustic data based on edge-preserving regularization has been proposed by introducing additional variables indicating the existence of an edge. Acoustic contrast, dielectric contrast and these edge markers are updated alternately.

Copyright (c) 2021 IEEE. Personal use is permitted. For any other purposes, permission must be obtained from the IEEE by emailing pubs-permissions@ieee.org.

This is the author's version of an article that has been published in this journal. Changes were made to this version by the publisher prior to publication.
The final version of record is available at http://dx.doi.org/10.1109/TCI.2021.3067158

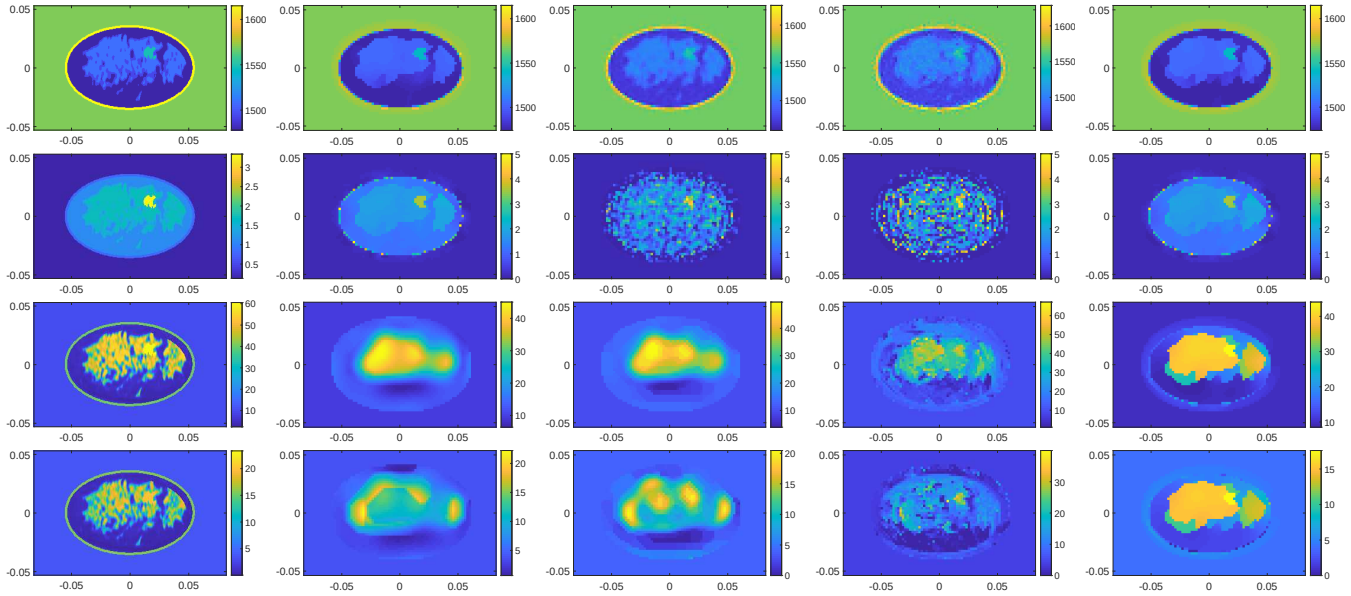

Fig. 7: Model 4 – Ground truth (1st column), separate reconstruction results of CSI-EP (2nd), MR-CSI (3rd) and joint inversion results of JCSI-CG (4th) and JCSI-EP (5th) with speed of sound c (1st row), attenuation α (2nd), real part ϵ_r' (3rd) and imaginary part ϵ_r'' (4th) of relative permittivity.

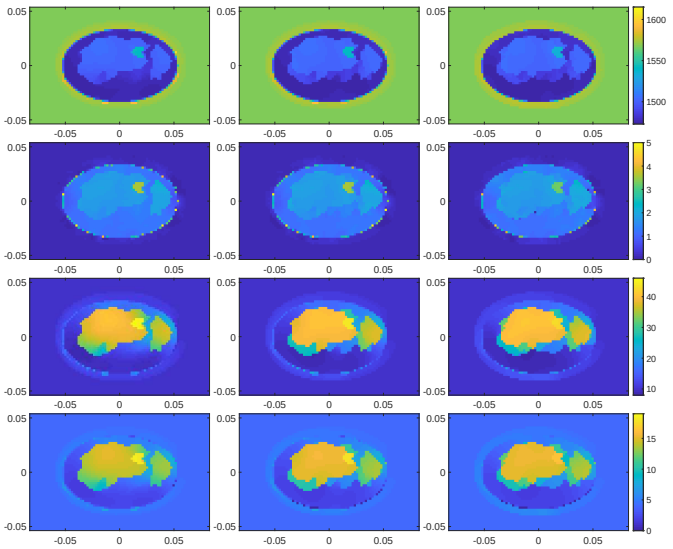

Fig. 8: Model 4 – Joint reconstruction results of speed of sound c (1st row), attenuation α (2nd), real part ϵ_r' (3rd) and imaginary part ϵ_r'' (4th) of relative permittivity by JCSI-EP with $\gamma = 0$ (left), $\gamma = 0.5$ (middle) and $\gamma = 5$ (right).

Comprehensive numerical experiments, with due comparison with approaches involving total variation or cross-gradient, show that by joint inversion, electromagnetic imaging can gain from the high resolution of acoustic imaging and map out small tumors, which is very difficult when electromagnetic data are the only ones involved. A good quality of acoustic data is required to get a satisfactory joint inversion result.

For the three realistic models as introduced, increasing the weight of electromagnetic data in updating the edge variables may decrease the contrast between the tumor and the background. Overall, the electromagnetic imaging quality is much enhanced by joint inversion however.

As for the choice of hyperparameters, here dealt with by thorough numerical experimentation beforehand, it still remains an open question. Forthcoming work should in particular focus onto a Bayesian methodology in order to estimate the hyperparameters jointly, so as to achieve a proper choice for each model under investigation.

REFERENCES

[1] A. E. Bulyshev, S. Y. Semenov, A. E. Souvorov, R. H. Svenson, A. G. Nazarov, Y. E. Sizov, and G. P. Tatsis, "Computational modeling of three-dimensional microwave tomography of breast cancer," *IEEE Transactions on Biomedical Engineering*, vol. 48, no. 9, pp. 1053–1056, 2001.

[2] J. D. Shea, P. Kosmas, S. C. Hagness, and B. D. Van Veen, "Three-dimensional microwave imaging of realistic numerical breast phantoms via a multiple-frequency inverse scattering technique," *Medical Physics*, vol. 37, no. 8, pp. 4210–4226, 2010.

[3] N. Ozmen-Eryilmaz, L. Demi, E. J. Alles, M. D. Verweij, and K. W. A. van Dongen, "Modeling acoustic wave field propagation in 3D breast models," in *2011 IEEE International Ultrasonics Symposium*, pp. 1700–1703, Oct 2011.

[4] N. Ozmen, R. Dapp, M. Zapf, H. Gemmeke, N. V. Ruiter, and K. W. van Dongen, "Comparing different ultrasound imaging methods for breast cancer detection," *IEEE Transactions on Ultrasonics, Ferroelectrics, and Frequency Control*, vol. 62, no. 4, pp. 637–646, 2015.

[5] N. Abdollahi, D. Kurrant, P. Mojabi, M. Omer, E. Fear, and J. LoVetri, "Incorporation of ultrasonic prior information for improving quantitative microwave imaging of breast," *IEEE Journal on Multiscale and Multiphysics Computational Techniques*, vol. 4, pp. 98–110, 2019.

[6] J. Asefi, A. Baran, and J. LoVetri, "An experimental phantom study for air-based quasi-resonant microwave breast imaging," *IEEE Transactions on Microwave Theory and Techniques*, vol. 67, no. 9, pp. 3946–3954, 2019.

[7] Y. Qin, T. Rodet, M. Lambert, and D. Lesselier, "Microwave breast imaging with prior ultrasound information," *IEEE Open Journal of Antennas and Propagation*, 2020.

[8] M. Omer, P. Mojabi, D. Kurrant, J. LoVetri, and E. Fear, "Proof-of-concept of the incorporation of ultrasound-derived structural information into microwave radar imaging," *IEEE Journal on Multiscale and Multiphysics Computational Techniques*, vol. 3, pp. 129–139, 2018.

Copyright (c) 2021 IEEE. Personal use is permitted. For any other purposes, permission must be obtained from the IEEE by emailing pubs-permissions@ieee.org.

This is the author's version of an article that has been published in this journal. Changes were made to this version by the publisher prior to publication.
The final version of record is available at http://dx.doi.org/10.1109/TCI.2021.3067158

[9] G. Gao, A. Abubakar, and T. M. Habashy, "Joint petrophysical inversion of electromagnetic and full-waveform seismic data," *Geophysics*, vol. 77, no. 3, pp. WA3–WA18, 2012.
[10] E. Haber and D. Oldenburg, "Joint inversion: a structural approach," *Inverse Problems*, vol. 13, no. 1, p. 63, 1997.
[11] L. A. Gallardo and M. A. Meju, "Characterization of heterogeneous near-surface materials by joint 2D inversion of DC resistivity and seismic data," *Geophysical Research Letters*, vol. 30, no. 13, 2003.
[12] L. A. Gallardo and M. A. Meju, "Joint two-dimensional DC resistivity and seismic travel time inversion with cross-gradients constraints," *Journal of Geophysical Research: Solid Earth*, vol. 109, no. B3, 2004.
[13] A. Abubakar, G. Gao, T. M. Habashy, and J. Liu, "Joint inversion approaches for geophysical electromagnetic and elastic full-waveform data," *Inverse Problems*, vol. 28, no. 5, p. 055016, 2012.
[14] W. Hu, A. Abubakar, and T. M. Habashy, "Joint electromagnetic and seismic inversion using structural constraints," *Geophysics*, vol. 74, no. 6, pp. R99–R109, 2009.
[15] T. Lan, H. Liu, N. Liu, J. Li, F. Han, and Q. H. Liu, "Joint inversion of electromagnetic and seismic data based on structural constraints using variational Born iteration method," *IEEE Transactions on Geoscience and Remote Sensing*, vol. 56, no. 1, pp. 436–445, 2017.
[16] Y. Zhang, Z. Zhao, Z. Nie, and Q. H. Liu, "Approach on joint inversion of electromagnetic and acoustic data based on structural constraints," *IEEE Transactions on Geoscience and Remote Sensing*, vol. 58, no. 11, pp. 7672–7681, 2020.
[17] E. Haber and M. H. Gazit, "Model fusion and joint inversion," *Surveys in Geophysics*, vol. 34, no. 5, pp. 675–695, 2013.
[18] X. Song, M. Li, F. Yang, S. Xu, and A. Abubakar, "Study on joint inversion algorithm of acoustic and electromagnetic data in biomedical imaging," *IEEE Journal on Multiscale and Multiphysics Computational Techniques*, vol. 4, pp. 2–11, 2019.
[19] L. I. Rudin, S. Osher, and E. Fatemi, "Nonlinear total variation based noise removal algorithms," *Physica D: nonlinear phenomena*, vol. 60, no. 1-4, pp. 259–268, 1992.
[20] L. Xu, C. Lu, Y. Xu, and J. Jia, "Image smoothing via L0 gradient minimization," in *Proceedings of the 2011 SIGGRAPH Asia Conference*, pp. 1–12, 2011.
[21] F. Zhu, Z. Liang, X. Jia, L. Zhang, and Y. Yu, "A benchmark for edge-preserving image smoothing," *IEEE Transactions on Image Processing*, vol. 28, no. 7, pp. 3556–3570, 2019.
[22] P. Lobel, C. Pichot, L. Blanc-Féraud, and M. Barlaud, "Microwave imaging: Reconstructions from experimental data using conjugate gradient and enhancement by edge-preserving regularization," *International Journal of Imaging Systems and Technology*, vol. 8, no. 4, pp. 337–342, 1997.
[23] C. Youzwishen and M. Sacchi, "Edge preserving imaging," *Journal of Seismic Exploration*, vol. 15, no. 1, p. 45, 2006.
[24] M. Belge, M. E. Kilmer, and E. L. Miller, "Wavelet domain image restoration with adaptive edge-preserving regularization," *IEEE Transactions on Image Processing*, vol. 9, no. 4, pp. 597–608, 2000.
[25] W. Gan, X. Wu, W. Wu, X. Yang, C. Ren, X. He, and K. Liu, "Infrared and visible image fusion with the use of multi-scale edge-preserving decomposition and guided image filter," *Infrared Physics & Technology*, vol. 72, pp. 37–51, 2015.
[26] P. Charbonnier, L. Blanc-Féraud, G. Aubert, and M. Barlaud, "Deterministic edge-preserving regularization in computed imaging," *IEEE Transactions on Image Processing*, vol. 6, no. 2, pp. 298–311, 1997.
[27] T. Hebert and R. Leahy, "A generalized EM algorithm for 3-D Bayesian reconstruction from Poisson data using Gibbs priors," *IEEE Transactions on Medical Imaging*, vol. 8, no. 2, pp. 194–202, 1989.
[28] C. Bouman and K. Sauer, "A generalized Gaussian image model for edge-preserving MAP estimation," *IEEE Transactions on Image Processing*, vol. 2, no. 3, pp. 296–310, 1993.
[29] S. Geman and D. E. McClure, "Bayesian image analysis: An application to single photon emission tomography," *Proceedings of the American Statistical Association*, pp. 12–18, 1985.
[30] S. Geman and D. Geman, "Stochastic relaxation, Gibbs distributions, and the Bayesian restoration of images," *IEEE Transactions on Pattern Analysis and Machine Intelligence*, no. 6, pp. 721–741, 1984.
[31] A. Blake and A. Zisserman, *Visual Reconstruction*. MIT Press, 1987.
[32] D. Geman and G. Reynolds, "Constrained restoration and the recovery of discontinuities," *IEEE Transactions on Pattern Analysis and Machine Intelligence*, vol. 14, no. 3, pp. 367–383, 1992.
[33] D. Geman and C. Yang, "Nonlinear image recovery with half-quadratic regularization," *IEEE Transactions on Image Processing*, vol. 4, no. 7, pp. 932–946, 1995.
[34] P. Charbonnier, L. Blanc-Féraud, and M. Barlaud, "ARTUR: An adaptive deterministic relaxation algorithm for edge-preserving tomographic reconstruction," *Res. Rep*, pp. 93–76, 1993.
[35] P. Charbonnier, L. Blanc-Feraud, G. Aubert, and M. Barlaud, "Two deterministic half-quadratic regularization algorithms for computed imaging," in *Proceedings of 1st International Conference on Image Processing*, vol. 2, pp. 168–172, IEEE, 1994.
[36] A. H. Delaney and Y. Bresler, "Globally convergent edge-preserving regularized reconstruction: an application to limited-angle tomography," *IEEE Transactions on Image Processing*, vol. 7, no. 2, pp. 204–221, 1998.
[37] P. M. Van Den Berg and R. E. Kleinman, "A contrast source inversion method," *Inverse Problems*, vol. 13, no. 6, p. 1607, 1997.
[38] E. Zastrow, S. K. Davis, M. Lazebnik, F. Kelcz, B. D. Van Veen, and S. C. Hagness, "Database of 3D grid-based numerical breast phantoms for use in computational electromagnetics simulations," tech. rep., Department of Electrical and Computer Engineering University of Wisconsin-Madison, 2008.
[39] P. M. van den Berg, A. Van Broekhoven, and A. Abubakar, "Extended contrast source inversion," *Inverse Problems*, vol. 15, no. 5, p. 1325, 1999.
[40] K. Belkebir, P. C. Chaumet, and A. Sentenac, "Superresolution in total internal reflection tomography," *Journal of the Optical Society A*, vol. 22, no. 9, pp. 1889–1897, 2005.
[41] T. D. Mast, "Empirical relationships between acoustic parameters in human soft tissues," *Acoustics Research Letters Online*, vol. 1, no. 2, pp. 37–42, 2000.
[42] P. M. Van den Berg and A. Abubakar, "Contrast source inversion method: State of art," *Progress in Electromagnetics Research*, vol. 34, pp. 189–218, 2001.
[43] P. M. van den Berg, A. Abubakar, and J. T. Fokkema, "Multiplicative regularization for contrast profile inversion," *Radio Science*, vol. 38, no. 2, 2003.
[44] Z. Wang, A. C. Bovik, H. R. Sheikh, and E. P. Simoncelli, "Image quality assessment: from error visibility to structural similarity," *IEEE Transactions on Image Processing*, vol. 13, no. 4, pp. 600–612, 2004.
[45] J. Nebeker and T. R. Nelson, "Imaging of sound speed using reflection ultrasound tomography," *Journal of Ultrasound in Medicine*, vol. 31, no. 9, pp. 1389–1404, 2012.
[46] M. Lazebnik, D. Popovic, L. McCartney, C. B. Watkins, M. J. Lindstrom, J. Harter, S. Sewall, T. Ogilvie, A. Magliocco, T. M. Breslin, *et al.*, "A large-scale study of the ultrawideband microwave dielectric properties of normal, benign and malignant breast tissues obtained from cancer surgeries," *Physics in Medicine & Biology*, vol. 52, no. 20, p. 6093, 2007.

Copyright (c) 2021 IEEE. Personal use is permitted. For any other purposes, permission must be obtained from the IEEE by emailing pubs-permissions@ieee.org.